Journal of Materials Chemistry A

COMMUNICATION

View Article Online
View Journal | View Issue

Cite this: J. Mater. Chem. A, 2017, 5, 1434

Received 23rd October 2016
Accepted 5th December 2016

DOI: 10.1039/c6ta09174a

www.rsc.org/MaterialsA

Hematite electron-transporting layers for environmentally stable planar perovskite solar cells with enhanced energy conversion and lower hysteresis†

Wei Hu,‡[ab] Tao Liu,‡[b] Xuewen Yin,[c] Hu Liu,[d] Xingyue Zhao,[c] Songping Luo,[c] Ying Guo,[b] Zhibo Yao,[c] Jinshu Wang,[b] Ning Wang,*[ab] Hong Lin*[c] and Zhanhu Guo*[d]

Non-obvious hysteresis and higher steady-state power conversion efficiency (PCE) were demonstrated by simply employing hematite (α-Fe_2O_3) as the electron transporting layer (ETL) to replace the conventional titania (TiO_2) ETL in planar heterojunction perovskite solar cells. The achieved higher built-in potential across the perovskite layer for the devices using α-Fe_2O_3 ETLs led to more efficient charge extraction/transport and less charge recombination than using TiO_2 ETLs. As a consequence, a significant reduction in the charge accumulation at the perovskite/α-Fe_2O_3 interface made the device much less sensitive to the scanning rate and direction, *i.e.*, lower hysteresis. Furthermore, α-Fe_2O_3 based devices displayed good stability over 30 days of storage time with exposure to ambient air, owing to the higher crystalline quality and uniform grain size of the perovskite films deposited on α-Fe_2O_3 ETLs than on TiO_2 ETLs.

1. Introduction

As third-generation solar cells, organometallic trihalide perovskite solar cells have advanced rapidly in only a few years after their invention, due to their low cost, high efficiency and straightforward architecture.[1] The power conversion efficiency (PCE) of perovskite cells has been increased from 9.7% (ref. 2) to 22.1% (ref. 3) with the usage of solid-state organic hole transport materials. To date, organometallic trihalide perovskites $CH_3NH_3PbX_3$ (X is iodine or a mixture of iodine, chlorine and bromine) have been regarded as the most promising light absorption materials for solar energy conversion due to their wide absorption range,[4] high extinction coefficient,[5] ambipolar charge transport,[6] and long electron–hole diffusion length.[7] These advantages have led to the development of planar perovskite solar cells (a typical planar architecture of SnO_2:F (FTO)/compact TiO_2/$CH_3NH_3PbI_3$/spiro-OMeTAD/Au), in which the mesoscopic layer consisting of TiO_2 nanoparticles (or nanowires[8]) has been replaced by a compact TiO_2 layer only, working as an electron transporting layer (ETL) and hole blocking layer. However, the TiO_2 based planar type device, though showing a high PCE above 19%,[9] has shown two major demerits, *i.e.*, mysterious hysteresis in current density–voltage (*J*–*V*) curves and poor durability of stable performance.[10,11] The hysteresis is observed to strongly depend on the device architecture, where perovskite devices with planar structures suffer from more obvious hysteresis behavior than mesoporous structure devices.[10] A lower PCE can be observed when operating planar devices in a forward scan (from short circuit (SC) to forward bias (FB)) than in the case of reverse scan (from FB to SC) in the *J*–*V* measurement.[10,12] The obvious hysteretic behavior has so far prevented a correct evaluation of their actual performance. The origin of hysteresis might be related to trapping/de-trapping of charge carriers,[13,14] changes in absorber or contact conductivity,[11] perovskite's ferroelectricity,[10,15–17] and ion migration.[18–20]

ETLs, a key component in high efficiency planar perovskite solar cells, need to have low charge transfer resistance and a matching energy level with the conduction band of the perovskite absorbing layer to offer a good electron extraction ability. However, planar perovskite solar cells with most widely used TiO_2 ETLs[21–23] suffer from serious hysteresis and inferior stability.[10–12] This hysteresis is mainly ascribed to both rich oxygen vacancies and electron traps on the TiO_2 surface.[24,25] The hysteresis can be reduced through the passivation of the TiO_2 layer with C60.[14,26] The passivation could minimize the trap states and improve electron transfer from $CH_3NH_3PbI_3$ to the TiO_2 ETL. On the other hand, TiO_2 was replaced by phenyl-C61-butyric acid

[a]State Key Laboratory of Marine Resource Utilization in South China Sea, Hainan University, Haikou 570228, P. R. China. E-mail: wangninguestc@gmail.com

[b]State Key Laboratory of Electronic Thin Film and Integrated Devices, University of Electronic Science and Technology of China, Chengdu 610054, P. R. China

[c]State Key Laboratory of New Ceramics & Fine Processing, School of Material Science and Engineering, Tsinghua University, Beijing 100084, China

[d]Integrated Composites Lab (ICL), Department of Chemical & Biomolecular Engineering, University of Tennessee, Knoxville, Tennessee, 37966, USA. E-mail: zguo10@utk.edu

† Electronic supplementary information (ESI) available. See DOI: 10.1039/c6ta09174a

‡ These authors contributed equally to this work.

methyl ester (PCBM) in perovskite devices with an inverted architecture to eliminate the hysteresis behaviour. PCBM could extract electrons more efficiently, thereby leading to less charge accumulation at the PCBM/$CH_3NH_3PbI_3$ interface, than conventional TiO_2 ETLs.[27] However, PCBM layers could be degraded through adsorption of oxygen or water in ambient air.[28] Although hematite (α-Fe_2O_3), the most stable iron oxide with n-type semiconducting properties under ambient conditions, has been used as an anode material for supercapacitors[29] as well as the photoanode of dye-sensitized solar cells to enhance the electron transfer rate,[30] its usage as an electron transporting layer to replace TiO_2 has not been reported. Herein, we employed low cost α-Fe_2O_3 for the first time as the ETL material instead of TiO_2 in planar perovskite cells. The charge accumulation at the perovskite/α-Fe_2O_3 interface is significantly reduced and thus is prominently effective to reduce the hysteresis. Furthermore, the fabricated solar cells demonstrate a good stability upon exposure to ambient air without any encapsulation.

2. Results and discussion

Fig. 1A and B present the top-view scanning electron microscopy (SEM) images of the Fe_2O_3/FTO and TiO_2/FTO, respectively. Both TiO_2 and Fe_2O_3 films exhibit a continuous and compact surface. Four XRD diffraction peaks of Fe_2O_3/FTO centered at 24.33, 33.28, 35.68 and 54.45°, Fig. 1C, are assigned to the (012), (104), (110) and (116) diffractions of α-Fe_2O_3, respectively.[31] Fig. 1D displays the Raman spectra of Fe_2O_3 films spun cast onto an (a) FTO substrate and (b) glass slide, in which seven optical modes of even symmetry ($2A_{1g} + 5E_{1g}$) associated with Fe_2O_3 as the hematite phase are observed for both samples. The top-view SEM images of the perovskite films on these two substrates exhibit crack-free coverage and flat surfaces, Fig. 1E and F. However, a closer inspection of the surface images suggests that a more uniform and larger grain size can be obtained for perovskite films grown on α-Fe_2O_3 ETLs than on TiO_2 ETLs. It is known that ETLs play the role of seeds for the halide perovskite precursor crystallizing on the substrate. To check the crystalline quality of the as-synthesized perovskite, XRD characterization was conducted for the hybrid perovskite deposited on both α-Fe_2O_3 and TiO_2 ETLs, Fig. 1G. The perovskite shows the typical peaks of the tetragonal phase and no diffraction peaks arising from PbI_2 are observed in both diffraction patterns. The diffraction peaks of the perovskite layer deposited on the α-Fe_2O_3 ETL are much stronger than those of the perovskite layer grown on the TiO_2 ETL, indicating

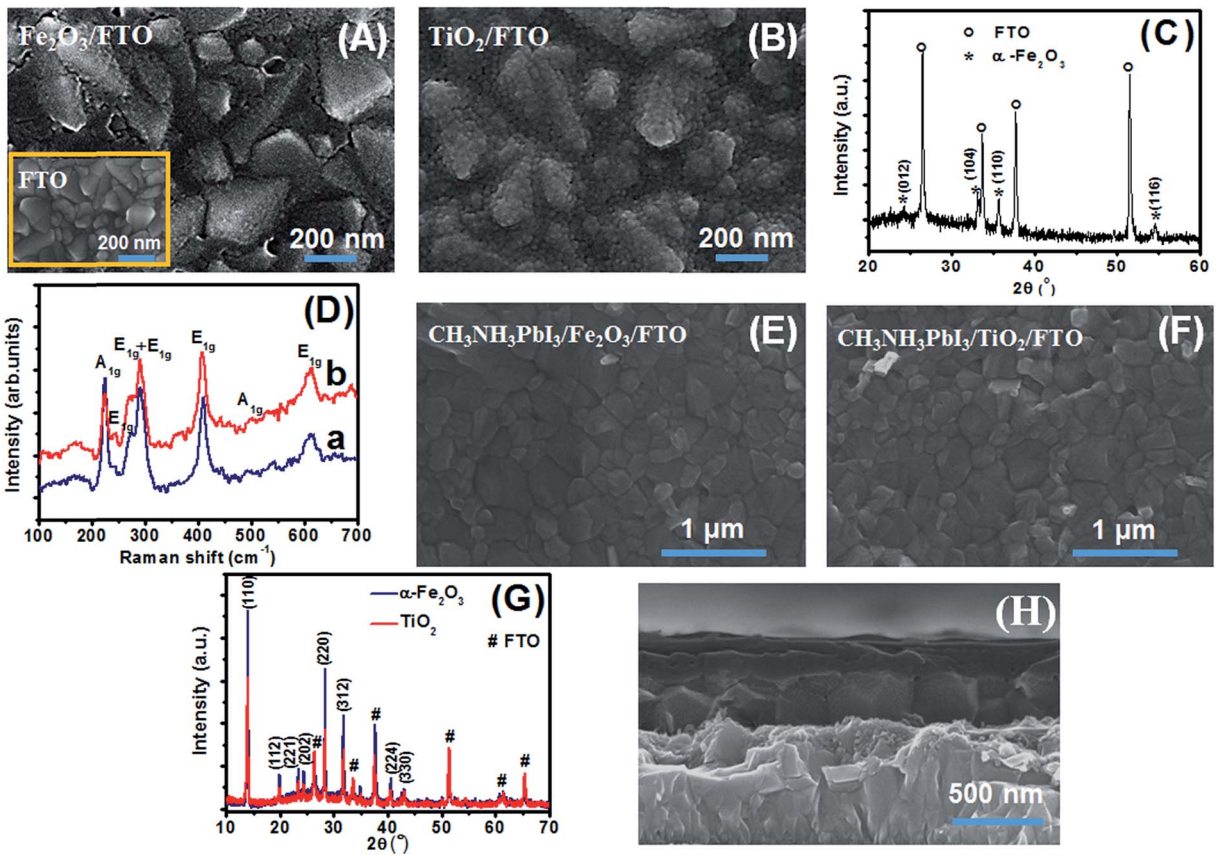

Fig. 1 Top view SEM images of the (A) α-Fe_2O_3/FTO thin film and (B) TiO_2/FTO thin film. Inset of (A) shows the typical surface morphology of the FTO substrate. (C) XRD spectrum of the α-Fe_2O_3/FTO film. (D) Raman spectra of α-Fe_2O_3 films grown on an (a) FTO substrate and (b) glass slide with an excitation wavelength of 488 nm at room temperature. The symmetry of the peaks in the hematite crystals is indicated. SEM surface images of the $CH_3NH_3PbI_3$ perovskite thin films deposited on (E) Fe_2O_3/FTO and (F) TiO_2/FTO substrates. (G) XRD patterns corresponding to perovskite films grown on (a) Fe_2O_3 and (b) TiO_2 coated FTO substrates. (H) SEM cross sectional image of the planar-heterojunction solar cell based on the Fe_2O_3 ETL.

that α-Fe_2O_3 favors crystallization and film formation of $CH_3NH_3PbI_3$. This may be induced by the growth of the crystals along different planes, possibly allowing denser packing and better coverage.

The direct current conductivity (σ) of the α-Fe_2O_3 and TiO_2 thin films was obtained by linear sweep voltammetry measurements, which were performed on the FTO/ETL/Au structure, Fig. S1A.† The *I–V* curves (Fig. S1B†) clearly illustrate that the σ value of α-Fe_2O_3 is almost three times as large as that of TiO_2, suggesting that the electron transporting properties of α-Fe_2O_3 are superior to those of TiO_2.[32] Fig. 1H shows a cross sectional image of a typical planar perovskite solar cell based on the α-Fe_2O_3 ETL. The α-Fe_2O_3 layer is only ~30 nm thick (Fig. S2A†) and cannot be seen clearly in Fig. 1H. Fig. S2B† shows the transmittance spectra of α-Fe_2O_3 and TiO_2 ETLs. Despite a relatively narrow band gap (2.2 eV) of α-Fe_2O_3, its ultra-thin thickness helps to decrease the absorption of incident light, thus leading to a slight decline in visible light transmittance as compared with the TiO_2 layer. Fig. S3† shows a cross-sectional view of a typical TiO_2 based planar perovskite solar cell, which has the same thickness of the hole transporting layer (HTL, ~230 nm) and perovskite active layer (~300 nm) as that of an α-Fe_2O_3 one.

Fig. 2A and B display the representative current density–voltage (*J–V*) curves of the planar devices with α-Fe_2O_3 and TiO_2 as ETLs, measured at different voltage sweep rates in the forward and reverse scans under AM 1.5G illumination (100 mW cm^{-2}). The corresponding photovoltaic parameters of the tested samples are listed in Table S1,† including short-circuit current density (J_{sc}), open-circuit voltage (V_{oc}), fill factor (FF) and PCE. Both devices show obvious hysteresis phenomena and the hysteresis becomes more pronounced with increasing the scanning rate. This hysteresis strongly influences the accurate performance evaluation of perovskite solar cells.[10,11] In our case, the performance of the TiO_2 based device is even more dependent on the scan rate and direction than that of the α-Fe_2O_3 based device. A high PCE (PCE = $(J \times V)_{max}/100$) of 15.32% was achieved for the TiO_2 based device only at a fast scanning rate (1 V s^{-1}) in a reverse scan. However, a reduced PCE (13.35%) was observed when the scan rate was reduced to 0.025 V s^{-1}. On the other hand, a drastic reduction of the PCE (irrespective of the scan rate) can be observed when operating the device in a forward scan instead of reverse scan (*e.g.* from 15.32% (reverse scan) down to 2.84% (forward scan) at a scan rate of 1 V s^{-1}), mainly attributed to the obvious decrease of the FF (FF = PCE × $100/(J_{sc} \times V_{oc})$), from 0.73 down to 0.18, Table S1.† In addition, the current density of the TiO_2 based device is observed to drop seriously with V_{oc} down to close to 0 when operating the device in a reverse scan at 0.1 and 0.025 V s^{-1}, *e.g.* from 19.5 mA cm^{-2} at 0.6 V down to 15.9 mA cm^{-2} at 0 V, Table S1.† Such hysteresis behaviors have been reported in other TiO_2 ETL based devices with planar and mesoporous structures[12,33,34] and are thought to be caused by a transient internal field formation on a time scale of seconds. These indicate that the TiO_2 based devices may lead to an erroneous PCE estimation if *J–V* characteristics are not judiciously reported. In contrast, the Fe_2O_3 based devices could effectively improve the hysteresis behavior. When the scan rate was reduced to 0.025 V s^{-1}, similar PCE values of 11.2% and

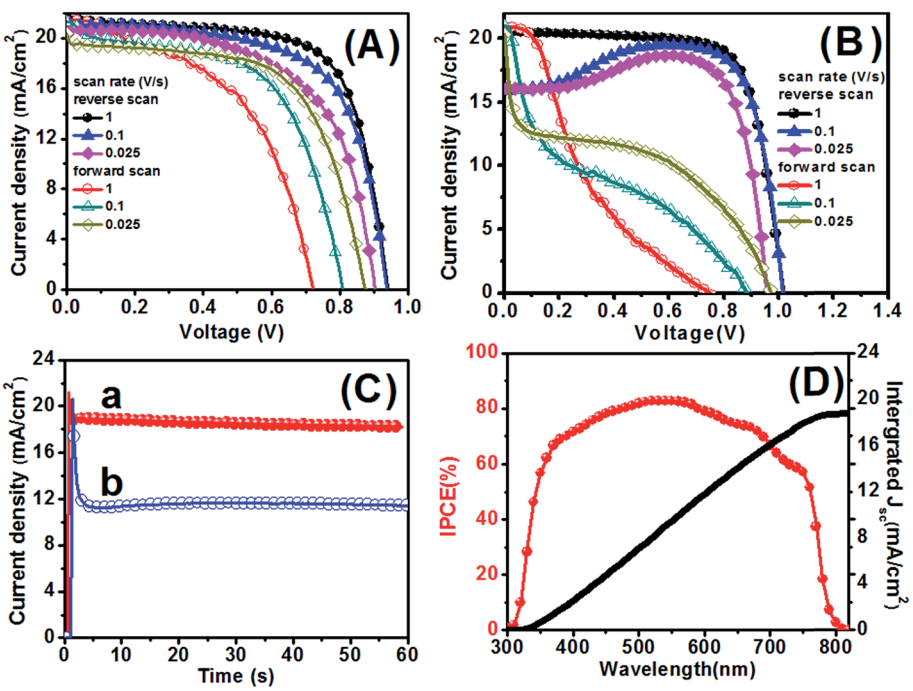

Fig. 2 *J–V* characteristics of planar perovskite solar cells employing (A) α-Fe_2O_3 and (B) TiO_2 ETLs measured with different scan rates and different scan directions under 1 sun AM 1.5G illumination. (C) Short-circuit current density transients during illumination for (a) α-Fe_2O_3 and (b) TiO_2 based devices. (D) IPCE spectrum of the planar perovskite solar cells based on the α-Fe_2O_3 ETL (red circles) and the integrated product of the IPCE spectrum with the AM 1.5G photon flux (black line).

10.7% (Table S1†) were achieved when operating the device in a reverse scan and forward scan, respectively.

Fig. 2C shows the transient behavior of J_{sc}. The J_{sc} of the device with the TiO_2 ETL, Fig. 2C(b), shows a drastic reduction over time, dropping from 20.6 to 11.4 mA cm^{-2}. However, there is a loss of *ca.* 2.2 mA cm^{-2} (from 21.17 to 18.95 mA cm^{-2}) for the α-Fe_2O_3 based device, Fig. 2C(a). In addition, the device with the α-Fe_2O_3 ETL can reach the steady state at a faster rate than the TiO_2 based solar cell, indicating much more efficient charge transfer of α-Fe_2O_3 devices than TiO_2 devices.[35] According to eqn (S1) for J_{sc} in the ESI,† the integrated incident photon-to-current efficiency (IPCE) (Fig. 2D) of the α-Fe_2O_3 based solar cells agrees well with the corresponding steady J_{sc} in Fig. 2C(a).

In addition, the α-Fe_2O_3 based solar cells present V_{oc} lower than those from TiO_2 based devices at the same scanning rate and scan direction, *i.e.* 0.94 V, Fig. 2A, for α-Fe_2O_3 and 1.02 V, Fig. 2B, for TiO_2. The V_{oc} can be derived from using eqn (1):[36]

$$V_{oc} \approx \frac{\left(\left|E^{HOMO}_{spiro\text{-}OMeTAD}\right| - \left|E^{LUMO}_{ETL}\right|\right)}{e} \quad (1)$$

where the HOMO (highest occupied molecular orbital) and LUMO (lowest unoccupied molecular orbital) are the valence-band maximum energy level and conduction band minimum energy level, respectively. Since both devices employ the same hole transporting layer (spiro-OMeTAD), the lower V_{oc} demonstrates a deeper conduction band minimum of α-Fe_2O_3 ($\sim$−4.5 eV) than that of TiO_2 ($\sim$−4.3 eV).[37]

The perovskite absorber layer is known to allow the photogenerated excitons to dissociate immediately into free electrons and holes when exposed to sunlight[38,39] and then drift and diffuse through the absorber and transport layers before being collected by the contact electrodes. Tao *et al.* have highlighted that the electron extraction strongly depends on the pre-polarization conditions in the presence of a flat TiO_2 ETL and further affects the device stability. Efficient charge extraction contributes to less sensitive performance to device polarization.[12] To obtain a deeper insight in the correlation between hysteresis behavior and charge extraction, the photoelectron spectra of TiO_2 and α-Fe_2O_3 were characterized, Fig. S4.† The work function of TiO_2 is 5.20 eV, very close to the reported value in ref. 40, which is larger than that of α-Fe_2O_3 (4.55 eV). It is known that $CH_3NH_3PbI_3$ perovskite is sandwiched in between selective contacts, resembling a p–i–n configuration.[33] Fig. 3A shows the corresponding energy diagram, where V_{bi} is the built-in potential across the absorber layer and acts as driving energy of carrier injection from the perovskite layer. Similar to a pn junction, the barrier height (qV_{bi}) of a p–i–n junction can be determined by the difference in the work function of the p-(HTL) and n-(ETL) layers.[41] Hence, the V_{bi} of the α-Fe_2O_3 based device is larger than that of the TiO_2 based one, indicating a stronger driving force for the charge injection from the $CH_3NH_3PbI_3$ perovskite crystal to the α-Fe_2O_3 ETL. To figure this out, Fig. 3B and C present the steady state photoluminescence (PL) spectra and time-resolved photoluminescence (TRPL) spectra of the perovskite layer spun cast on different substrates, respectively, which can reveal the photogenerated charge transfer and charge recombination loss. The obvious emission peaks of $CH_3NH_3PbI_3$ at around 770 nm are observed, Fig. 3B. Owing to the energy mismatch of the conduction bands of Al_2O_3 and $CH_3NH_3PbI_3$, the electron injection is not feasible[38] and thus the corresponding PL spectra (see Fig. 3B(c)) should reflect natural recombination events. However, the obvious quenching in PL emission suggests an efficient charge dissociation between $CH_3NH_3PbI_3$ and the ETL. The emission peak in the α-Fe_2O_3 ETL, Fig. 3B(a), is quenched to a lower level than that in the TiO_2 ETL, Fig. 3B(b), suggesting that the photogenerated electrons can be extracted to the α-Fe_2O_3 ETL more quickly than those of the TiO_2 one before bulk recombination.[26] This is in agreement with the fact that a larger built-in potential across the perovskite layer allows for a more efficient charge injection for the α-Fe_2O_3 device.

To further study the charge transfer kinetic process, the TRPL spectra of the $CH_3NH_3PbI_3$ perovskite layer grown on TiO_2, α-Fe_2O_3 and Al_2O_3 substrates were characterized, Fig. 3C. The PL lifetime of the samples was fitted to a bi-exponential decay function containing a fast decay and a slow decay process, eqn (2).[42]

$$f(t) = \sum_i A_i \exp(-t/\tau_i) + K \quad (2)$$

where A_i is the decay amplitude, τ_i is the decay time and K is a constant for the base-line offset. The fast decay process is largely attributed to the charge carrier extraction across the interface between $CH_3NH_3PbI_3$ and ETLs, and the slow decay process corresponds to the result of radiative decay.[43] The fitting parameters are summarized in Table S2.† The Al_2O_3 based device, Fig. 3C(c), exhibits the longest PL decay time up to $\tau_1 =$ 16.84 ns and $\tau_2 = 2.24$ ns. The PL decay time of the TiO_2 device, Fig. 3C(b), is found to be $\tau_1 = 12.58$ ns and $\tau_2 = 0.99$ ns, the corresponding amplitudes are 29.41% and 70.59%. The τ_1 and τ_2 of the Fe_2O_3 based device, Fig. 3C(a), drop to 8.29 ns and 0.77 ns, respectively, and the amplitude of the relatively fast decay time increases to 75.00%. Herein, the average recombination time (τ_{ave}) is estimated with the τ_i and A_i values according to eqn (3).[44]

$$\tau_{ave} = \frac{\sum A_i \tau_i^2}{\sum A_i \tau_i} \quad (3)$$

As listed in Table S1,† the τ_{ave} using the TiO_2 ETL is 12.58 ns close to that of the Al_2O_3 case (12.70 ns), suggesting that the TiO_2 ETL failed to significantly improve the electron injection from the perovskite. However, the obvious decrease of τ_{ave} (6.65 ns) is achieved when the α-Fe_2O_3 ETL is used. These changes in the decay time clearly demonstrate that the electrons transfer faster from the perovskite layer to the α-Fe_2O_3 ETL than in the case of the TiO_2 ETL, which is in agreement with the steady state PL measurement results (see Fig. 3B). It is apparent that a stronger steady state PL quenching and more efficient charge injection can be achieved for $CH_3NH_3PbI_3$/α-Fe_2O_3 due to the relatively larger V_{bi} across the perovskite layer. In contrast, the poor charge transfer from the perovskite interfaces

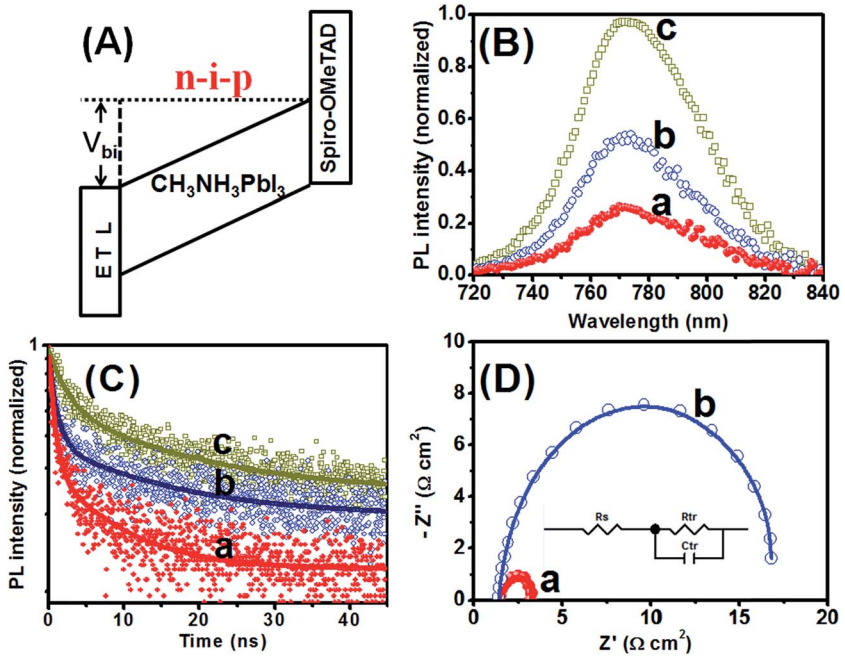

Fig. 3 (A) The energy diagram of perovskite solar cells with a typical p–i–n structure. (B) Steady-state PL emission spectra and (C) TRPL decay curves of the $CH_3NH_3PbI_3$ perovskite films deposited on different ETLs, scatter points are from experimental data, and the solid line is the corresponding fitting curve. (D) Nyquist plot of perovskite solar cells with different ETLs at an applied voltage of 0.7 V under 1 sun conditions. The inset in (D) gives the corresponding equivalent circuit model used for fitting the Nyquist plots. (a) α-Fe_2O_3 ETL, (b) TiO_2 ETL, and (c) Al_2O_3 ETL.

to the TiO_2 ETL will cause charge accumulation at the $CH_3NH_3PbI_3/TiO_2$ interfaces, which could ultimately result in a serious hysteresis.[14,24,25]

Furthermore, electrical impedance spectroscopy (EIS) was performed to study the interfacial charge transport in the perovskite solar cells with different ETLs. As shown in Fig. 3D, the only arc appeared in the high frequency region (2 MHz to 100 mHz) is associated with the transfer resistance (R_{tr}) at the perovskite/ETL and HTL/perovskite interfaces.[45] The Nyquist plot was fitted to an appropriate equivalent circuit model (see the inset of Fig. 3D),[45,46] and the related fitting parameters are summarized in Table S3.† Owing to the same HTL (spiro-OMeTAD) used in our case, R_{tr} reflects the electron transport properties at the perovskite/ETL interface. The device with the α-Fe_2O_3 ETL (Fig. 3D(a)) exhibits a smaller R_{tr} of 1.63 Ω cm^2 than that using the TiO_2 ETL (15.19 Ω cm^2 in Fig. 3D(b)). A smaller R_{tr} implies more efficient extraction/transport of electrons at the $CH_3NH_3PbI_3$/ETL interface, which is in agreement with the analysis results of the steady state PL and TRPL.

For a direct comparison of the steady-state behavior of perovskite solar cells based on the α-Fe_2O_3 and TiO_2 ETLs, Fig. 4A presents the stabilized J_{sc} (J_m) and power output close to the maximum power point (PCE_m), which is measured as a function of time at a forward bias set (V_m). The voltage at the maximum power point is 0.75 V for TiO_2 ETLs and 0.65 V for α-Fe_2O_3 ETLs. The α-Fe_2O_3 based device exhibits a higher stable PCE_m ($PCE_m = (V_m \times J_m)$%) value as high as 10.78% than the TiO_2 based one (6.37%). According to the *J–V* curves, however, the device with the TiO_2 ETL delivers the highest PCE of 15.32%, Table S1.† The opposite results further illustrate that *J–V* characteristics cannot give a reliable photovoltaic performance of the planar perovskite solar cells in our case. As aforementioned, this poor performance of the TiO_2 based device is mainly due to the loss of steady-state photocurrent (Fig. 2C). Furthermore, Fig. S5A† shows the thickness-dependent PCE_m, indicating that the optimized thickness of the α-Fe_2O_3 film is 30 nm for maximum photovoltaic performance. A thinner α-Fe_2O_3 layer (~20 nm) could help improve the transmittance of visible light, which contributes to more light absorption by the perovskite film, Fig. S5B.† However, the ultrathin film (<20 nm) with continuous and crack-free coverage is very hard to achieve by a spin-coating process. This could induce significant charge recombination at the interface of the perovskite and the partially exposed FTO, thus leading to reduced photovoltaic performance of the device with a 20 nm-thick α-Fe_2O_3 ETL.

The performances of planar hetero-junction perovskite solar cells based on either TiO_2 or ZnO ETLs are unstable over time and significantly degraded to 10–30% of the initial PCE after only dozens of hours of storage,[9,47] no matter what atmosphere the devices are stored in.[9,46] In this regard, it is necessary to explore the air stability of α-Fe_2O_3 based planar perovskite solar cells without encapsulation, Fig. 4B. It is obvious that the device using conventional TiO_2 ETLs presents worse air stability and degrades to <50% of its initial PCE within 15 days of storage in ambient air. In contrast, the PCE of the α-Fe_2O_3 based device remains almost the same as its initial value even after 30 days of storage in ambient air. For planar perovskite solar cells, the formation of uniform and compact perovskite films is very crucial to their long-term stability.[48] The high crystalline quality of perovskite films grown on α-Fe_2O_3 ETLs contributes to the

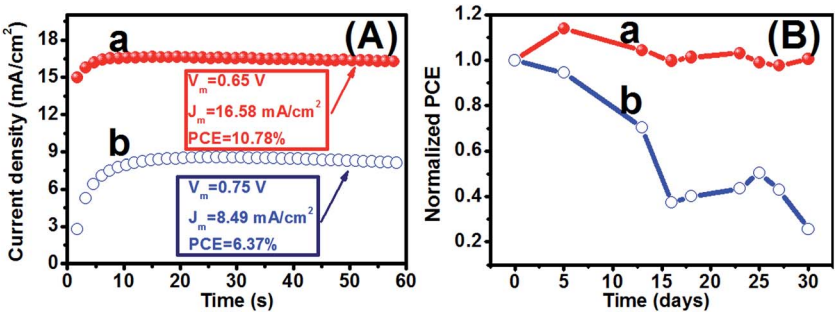

Fig. 4 (A) Stabilized current density and power output measured close to the maximum power point for planar perovskite solar cells biased at 0.65 V for (a) the α-Fe_2O_3 ETL and 0.75 V for (b) the TiO_2 ETL. (B) Normalized PCE of planar perovskite solar cells based on α-Fe_2O_3 and TiO_2 ETLs as a function of storage time in ambient air.

formation of a uniform film, and thus suppresses the decomposition of adjacent moisture-sensitive perovskite films. Besides, non-radiative charge recombination among the perovskite grain boundaries could result in the degradation of device stability.[49] Hence, the existence of a large number of small-size grains for perovskite films grown on TiO_2 ETLs is unfavorable to environmental stability.

3. Conclusions

In summary, we have described a significantly enhanced steady-state PCE and less hysteresis behaviour of a $CH_3NH_3PbI_3$ based planar-heterojunction perovskite solar cell with an α-Fe_2O_3 thin film as the ETL than that using a conventional TiO_2 ETL. Benefiting from larger V_{bi} across the perovskite absorber layer, the α-Fe_2O_3 based device provides a stronger driving force to facilitate charge extraction/transport and suppress carrier recombination compared to the TiO_2 based device, as witnessed by the analysis results of steady-state PL, TRPL and EIS. A significant reduction in the charge accumulation at the perovskite/α-Fe_2O_3 interface makes the device much less sensitive to the scanning rate and direction. Finally, the fabricated solar cells with α-Fe_2O_3 ETLs present a good stability upon exposure to ambient air without any encapsulation, which is expected to promote the development of novel perovskite photovoltaic technology.

4. Experimental section

4.1 Preparation of α-Fe_2O_3 and TiO_2 ETLs

Prior to the deposition of the ETL, fluorine-doped tin oxide (FTO)-coated glass sheets were etched with zinc powder and HCl (2 M) to obtain the required electrode pattern. The etched FTO substrates were then sonicated sequentially with detergent, distilled water, ethanol, acetone and 2-propanol for 15 min. The dried substrates were finally treated with UV-ozone for 15 min. 0.1 M $Fe(NO_3)_3 \cdot 9H_2O$ dissolved in ethanol was spun on the as-cleaned FTO glass at 6000 rpm for 40 s, followed by sintering at 500 °C for 1 h to form a thin α-Fe_2O_3 compact layer. For comparison, a TiO_2 compact layer was also spin-coated on FTO glass at 2000 rpm for 40 s using the precursor solution consisting of 350 μL titanium isopropoxide dissolved in 5 mL ethanol, and then sintered at 500 °C for 0.5 h.

4.2 Device fabrication

Before $CH_3NH_3PbI_3$ fabrication, methyl ammonium iodide (CH_3NH_3I) was first synthesized. In short, CH_3NH_3I crystals can be obtained through the reaction of 24 mL methylamine and 10 mL hydroiodic acid in a 100 mL round bottomed flask at 0 °C under stirring for 2 h. Then the precipitate was recovered by evaporation at 80 °C for 2 h and subsequently washed with diethyl ether under stirring for 30 min. Then, this was repeated twice, and snow-white CH_3NH_3I crystals were successfully synthesized by drying at 60 °C in a vacuum oven for 24 h. A mixture of the as-prepared CH_3NH_3I (0.200 g) and PbI_2 (0.578 g) was dissolved in 1 mL anhydrous *N*,*N*-dimethylformamide (DMF), followed by stirring at room temperature for 20 min to produce a clear $CH_3NH_3PbI_3$ solution with a concentration of 45 wt%. A $CH_3NH_3PbI_3$ perovskite film was prepared on an Fe_2O_3 (TiO_2) coated FTO substrate by spin coating 70 μL $CH_3NH_3PbI_3$ solution at 5000 rpm for 40 seconds. 180 μL of anhydrous chlorobenzene was quickly dropped onto the surface during this process, leading to the color change of the film into dark brown. To remove the excess of reagents, the obtained perovskite film was immediately placed on a hot plate at 100 °C for 15 min. The hole-transporting material was subsequently spin cast on the perovskite layer by spin coating a solution mixture (4000 rpm for 40 s), which was prepared by adding 72.3 mg 2,2′,7,7′-tetrakis(*N*,*N*-di-*p*-methoxyphenylamine)-9,9′-spirobifluorene (spiro-OMeTAD), 28.8 μL 4-*tert*-butylpyridine (TBP) and 17.5 μL stock solution consisting of 520 mg mL^{-1} lithium bis(trifluoromethylsulphonyl)imide (Li-TFSI) in acetonitrile to 1 mL chlorobenzene. Finally, the device was fabricated by thermal evaporation of a 50 nm-thick gold film as the top anode. All the devices were stored in a drying oven overnight and tested the next day.

4.3 Device characterization

X-ray diffraction (XRD) pattern data were recorded by high resolution X-ray diffraction (HRXRD) using a Bede D1 X-ray diffractometer. Raman spectra were obtained using a Dilor XY spectrometer and multichannel CCD detector with a 488 nm

line of an Ar^+ laser operating at room temperature. The morphology of the samples was characterized with a Zeiss Merlin scanning electron microscope (SEM). The work function of Fe_2O_3 and TiO_2 was measured by photoelectron emission spectroscopy using a Riken-AC2 photo-electron spectrometer in air. The photocurrent density–voltage (*J–V*) characteristics of the solar cell were evaluated with a digital source meter (2400, Keithley Instruments, USA) under AM 1.5G illumination (100 mW cm^{-2}), which was realized by using a solar simulator (91192, Oriel, USA) and calibrated by using a standard silicon solar cell before measurement. The incident photon to current efficiency (IPCE) was determined by using a solar cell quantum efficiency measurement system (QEX10, PV measurements, USA). EIS was performed by using a Zahner system (Zahner, Zahner-Electrik GmbH&Co. KG, Germany) and the Z-view software was used to analyze the impedance data. The steady-state photoluminescence (PL) emission spectra and time resolved PL (TRPL) decay spectra were measured by using a fluorescence spectrometer instrument (FLS920, Edinburgh Instruments, Livingston, UK). A picosecond pulsed diode laser with an excitation wavelength of 405 nm was used to record the emission decay curves. A 450 W ozone-free xenon lamp was used for steady-state PL measurements. The hydrophobicity of the Fe_2O_3 thin film and TiO_2 thin film was determined by contact angle measurements (CTA480).

Acknowledgements

China-Japan International Cooperation Program Funds (No. 2010DFA61410 and 2011DFA50530), the National Natural Science Foundation of China (No. 51272037, 51272126, 51303116 and 51472043), the Program for New Century Excellent Talents in University (No. NCET-12-0097) and Fundamental Research Funds for the Central Universities (No. ZYGX2015KYQD039) are acknowledged for financial support.

Notes and references

1 J. Berry, T. Buonassisi, D. A. Egger, G. Hodes, L. Kronik, Y. L. Loo, I. Lubomirsky, S. R. Marder, Y. Mastai, J. S. Miller, D. B. Mitzi, Y. Paz, A. M. Rappe, I. Riess, B. Rybtchinski, O. Stafsudd, V. Stevanovic, M. F. Toney, D. Zitoun, A. Kahn, D. Ginley and D. Cahen, *Adv. Mater.*, 2015, **27**, 5102.
2 H. S. Kim, C. R. Lee, J. H. Im, K. B. Lee, T. Moehl, A. Marchioro, S. J. Moon, R. Humphry-Baker, J. H. Yum, J. E. Moser, M. Gratzel and N. G. Park, *Sci. Rep.*, 2012, **2**, 591.
3 Research Cell Efficiency Records, NREL, http://www.nrel.gov/ncpv/, accessed, April 2016.
4 Y. Ogomi, A. Morita, S. Tsukamoto, T. Saitho, N. Fujikawa, Q. Shen, T. Toyoda, K. Yoshino, S. S. Pandey, T. Ma and S. Hayase, *J. Phys. Chem. Lett.*, 2014, **5**, 1004.
5 S. Kazim, M. K. Nazeeruddin, M. Grätzel and S. Ahmad, *Angew. Chem., Int. Ed.*, 2014, **53**, 2812.
6 J. M. Ball, M. M. Lee, A. Hey and H. J. Snaith, *Energy Environ. Sci.*, 2013, **6**, 1739.
7 Q. Dong, Y. Fang, Y. Shao, P. Mulligan, J. Qiu, L. Cao and J. Huang, *Science*, 2015, **347**, 967.
8 Q. Jiang, X. Sheng, Y. Li, X. Feng and T. Xu, *Chem. Commun.*, 2014, **50**, 14720.
9 H. Zhou, Q. Chen, G. Li, S. Luo, T. B. Song, H. S. Duan, Z. Hong, J. You, Y. Liu and Y. Yang, *Science*, 2014, **345**, 542.
10 H. J. Snaith, A. Abate, J. M. Ball, G. E. Eperon, T. Leijtens, N. K. Noel, S. D. Stranks, J. T. Wang, K. Wojciechowski and W. Zhang, *J. Phys. Chem. Lett.*, 2014, **5**, 1511.
11 E. L. Unger, E. T. Hoke, C. D. Bailie, W. H. Nguyen, A. R. Bowring, T. Heumüller, M. G. Christoforo and M. D. McGehee, *Energy Environ. Sci.*, 2014, **7**, 3690.
12 C. Tao, S. Neutzner, L. Colella, S. Marras, A. R. S. Kandada, M. Gandini, M. D. Bastiani, G. Pace, L. Manna, M. Caironi, C. Bertarelli and A. Petrozza, *Energy Environ. Sci.*, 2015, **8**, 2365.
13 T. Heiser and E. R. Weber, *Phys. Rev. B: Condens. Matter Mater. Phys.*, 1998, **58**, 3893.
14 K. Wojciechowski, S. D. Stranks, A. Abate, G. Sadoughi, A. Sadhanala, N. Kopidakis, G. Rumbles, C. Li, R. H. Friend, A. K. Jen and H. J. Snaith, *ACS Nano*, 2014, **8**, 12701.
15 A. Dualeh, T. Moehl, N. Tetreault, J. Teuscher, P. Gao, M. K. Nazeeruddin and M. Grätzel, *ACS Nano*, 2013, **8**, 362.
16 J. M. Frost, K. T. Butler, F. Brivio, C. H. Hendon, M. Van-Schilfgaarde and A. Walsh, *Nano Lett.*, 2014, **14**, 2584.
17 C. C. Stoumpos, C. D. Malliakas and M. G. Kanatzidis, *Inorg. Chem.*, 2013, **52**, 9019.
18 C. Eames, J. M. Frost, P. R. Barnes, B. C. O'regan, A. Walsh and M. S. Islam, *Nat. Commun.*, 2015, **6**, 7497.
19 Y. Yuan, J. Chae, Y. Shao, Q. Wang, Z. Xiao, A. Centrone and J. Huang, *Adv. Energy Mater.*, 2015, **5**, 1500615.
20 Z. Xiao, Y. Yuan, Y. Shao, Q. Wang, Q. Dong, C. Bi, P. Sharma, A. Gruverman and J. Huang, *Nat. Mater.*, 2015, **14**, 193.
21 P. Docampo, F. C. Hanusch, S. D. Stranks, M. Döblinger, J. M. Feckl, M. Ehrensperger, N. K. Minar, M. B. Johnston, H. J. Snaith and T. Bein, *Adv. Energy Mater.*, 2014, **4**, 1400355.
22 Q. Luo, Y. Zhang, C. Liu, J. Li, N. Wang and H. Lin, *J. Mater. Chem. A*, 2015, **3**, 15996.
23 P. You, Z. Liu, Q. Tai, S. Liu and F. Yan, *Adv. Mater.*, 2015, **27**, 3632.
24 H. S. Kim, I. H. Jang, N. Ahn, M. Choi, A. Guerrero, J. Bisquert and N. G. Park, *J. Phys. Chem. Lett.*, 2015, **6**, 4633.
25 B. Wu, K. Fu, N. Yantara, G. Xing, S. Sun, T. C. Sum and N. Mathews, *Adv. Energy Mater.*, 2015, **5**, 1500829.
26 Y. Hou, C. O. R. Quiroz, S. Scheiner, W. Chen, T. Stubhan, A. Hirsch, M. Halik and C. J. Brabec, *Adv. Energy Mater.*, 2015, **5**, 1501056.
27 J. Y. Jeng, Y. F. Chiang, M. H. Lee, S. R. Peng, T. F. Guo, P. Chen and T. C. Wen, *Adv. Mater.*, 2013, **25**, 3727.
28 Q. Bao, X. Liu, S. Braun and M. Fahlman, *Adv. Energy Mater.*, 2014, **4**, 1301272.
29 H. Wang, Z. Xu, H. Yi, H. Wei, Z. Guo and X. Wang, *Nano Energy*, 2014, **7**, 86.
30 H. Niu, S. Zhang, Q. Ma, S. Qin, L. Wan, J. Xu and S. Miao, *RSC Adv.*, 2013, **3**, 17228.

31 J. Chen, L. Xu, W. Li and X. L. Gou, *Adv. Mater.*, 2005, **17**, 582.
32 K. Wang, Y. Shi, Q. Dong, Y. Li, S. Wang, X. Yu, M. Wu and T. Ma, *J. Phys. Chem. Lett.*, 2015, **6**, 755.
33 W. Tress, N. Marinova, T. Moehl, S. M. Zakeeruddin, M. K. Nazeeruddin and M. Grätzel, *Energy Environ. Sci.*, 2015, **8**, 995.
34 Y. H. Lee, J. Luo, R. Humphry-Baker, P. Gao, M. Grätzel and M. K. Nazeeruddin, *Adv. Funct. Mater.*, 2015, **25**, 3925.
35 K. Yan, Z. Wei, J. Li, H. Chen, Y. Yi, X. Zheng, X. Long, Z. Wang, J. Wang, J. Xu and S. Yang, *Small*, 2015, **11**, 2269.
36 S. Y. Sun, T. Salim, N. Mathews, M. Duchamp, C. Boothroyd, G. C. Xing, T. C. Sum and Y. M. Lam, *Energy Environ. Sci.*, 2014, **7**, 399.
37 M. Grätzel, *Nature*, 2001, **414**, 338.
38 M. M. Lee, J. Teuscher, T. Miyasaka, T. N. Murakami and H. J. Snaith, *Science*, 2012, **338**, 643.
39 V. D'Innocenzo, G. Grancini, M. J. P. Alcocer, A. R. S. Kandada, S. D. Stranks, M. M. Lee, G. Lanzani, H. J. Snaith and A. Petrozza, *Nat. Commun.*, 2014, **5**, 3586.
40 S. Gutmann, M. A. Wolak, M. Conrad, M. M. Beerbom and R. Schlaf, *J. Appl. Phys.*, 2010, **107**, 103705.
41 S. Olthof, H. Kleemann, B. Lüssem and K. Leo, *Mater. Res. Soc. Symp. Proc.*, 2010, **1270**, 1270-II09-49.
42 D. Yang, R. Yang, J. Zhang, Z. Yang, S. Liu and C. Li, *Energy Environ. Sci.*, 2015, **8**, 3208.
43 P. W. Liang, C. Y. Liao, C. C. Chueh, F. Zuo, S. T. Williams, X. K. Xin, J. Lin and A. K. Y. Jen, *Adv. Mater.*, 2014, **26**, 3748.
44 S. Gonzalez-Carrero, R. E. Galian and J. Perez-Prieto, *J. Mater. Chem. A*, 2015, **3**, 9187.
45 Z. Wei, H. Chen, K. Yan, X. Zheng and S. Yang, *J. Mater. Chem. A*, 2015, **3**, 24226.
46 X. Xu, Z. Liu, Z. Zuo, M. Zhang, Z. Zhao, Y. Shen, H. Zhou, Q. Chen, Y. Yang and M. Wang, *Nano Lett.*, 2014, **15**, 2402.
47 D. Liu, J. Yang and T. L. Kelly, *J. Am. Chem. Soc.*, 2014, **136**, 17116.
48 Y. Wang, N. Song, L. Feng and X. Deng, *ACS Appl. Mater. Interfaces*, 2016, **8**, 24703.
49 Q.-Q. Ge, J. Ding, J. Liu, J.-Y. Ma, Y.-X. Chen, X.-X. Gao, L.-J. Wan and J.-S. Hu, *J. Mater. Chem. A*, 2016, **4**, 13458.